

Semantic Segmentation of Anomalous Diffusion Using Deep Convolutional Networks

Xiang Qu,¹ Yi Hu,² Wenjie Cai,¹ Yang Xu,² Hu Ke,² Guolong Zhu,¹ and Zihan Huang^{1,*}

¹*School of Physics and Electronics, Hunan University, Changsha 410082, China*

²*Hubei Medical Devices Quality Supervision and Test Institute, Wuhan 430075, China*

Heterogeneous dynamics commonly emerges in anomalous diffusion with intermittent transitions of diffusion states but proves challenging to identify using conventional statistical methods. To capture these transient changes of dynamics more effectively, we propose a data-driven approach and design a deep learning model (U-AnDi) based on the convolutional neural network (CNN) for the semantic segmentation of anomalous diffusion trajectories. This model is developed within the framework of the 1D CNN and U-Net, incorporating a network encoder derived from our previous work, known as WADNet. Two subtasks with respect to the segmentation of trajectories are addressed in this work, focusing on those with varying diffusion exponents and dynamics models, respectively. Without requiring any prior knowledge of anomalous diffusion, our method achieves an excellent performance for both tasks on simulated trajectories. The validation results show a mean absolute error (MAE) of the order of 0.01 in predicting diffusion exponents, and an mDice coefficient approaching 1 in segmenting dynamics models. In contrast, other methods such as recurrent neural networks or Transformers are unable to achieve similar performance levels. In particular, our model is also examined using real-world anomalous diffusion data: the diffusion of transmembrane proteins on cell membrane surfaces, and the segmentation results are highly consistent with experimental observations. Our findings could offer a heuristic deep learning solution for the detection of heterogeneous dynamics in single-molecule/particle tracking experiments, and have the potential to be generalized as a universal scheme for time-series segmentation.

I. INTRODUCTION

Anomalous diffusion [1, 2], characterized by the non-linear transport phenomena that deviate from standard Brownian motion, has drawn significant attention due to its widespread occurrence in various scientific fields, such as physics [3–7], chemistry [8–11], biology [12–16], and finance [17–19]. Since anomalous diffusion can provide valuable insights into the underlying mechanisms of complex systems, it is of great importance to perform accurate and reliable analysis of this phenomenon [20–32]. However, due to the heterogeneous dynamics with intermittent transitions of diffusion states [33–36], conventional statistical methods usually fail to precisely describe the anomalous diffusion processes in real-world experimental environments. This emphasizes the necessity of exploring effective techniques for the semantic segmentation of anomalous diffusion trajectories, which could offer a more fine-grained approach to detect state transitions and distinguish heterogeneous behaviors in diffusion dynamics.

On the other hand, as a pivotal technique in computer vision, semantic segmentation makes pixel-wise predictions in an image to enable the identification and delineation of distinct regions [37]. With the advent of deep learning techniques, semantic segmentation methods have experienced a rapid development in recent years, significantly outperforming traditional approaches that rely on handcrafted features [38–44]. These deep-learning-based methods have demonstrated remarkable success in a wide array of applications, including object

recognition [38–40], scene understanding [41], and medical image analysis [42–44]. In particular, convolutional neural networks (CNNs) have shown unparalleled capabilities in capturing complex patterns and hierarchical representations from raw data, leading to state-of-the-art results in various semantic segmentation tasks [37]. One representative example is the U-Net architecture [42], which is built on the basis of an encoder-decoder structure of CNNs and rational use of skip connections. U-Net has emerged as one of the most popular and effective frameworks for semantic segmentation and proven to be highly effective in diverse segmentation tasks [44]. Therefore, CNNs have demonstrated considerable promise in tackling the semantic segmentation problem of anomalous diffusion.

In this work, motivated by the successful applications of CNNs in semantic segmentation, we investigate the potential of employing deep convolutional networks for the semantic segmentation of anomalous diffusion. By incorporating a 1D-CNN encoder derived from our previous work (WADNet) [45] into the U-Net framework, we design a deep learning model, named U-AnDi, which can accurately identify transient changes of diffusion states from raw trajectory data. The effectiveness of U-AnDi is examined through two distinct subtasks, each focusing on the segmentation of trajectories with varying diffusion exponents and dynamics models, respectively. By leveraging the powerful feature extraction capabilities of WADNet encoder for time-series data and the well-established U-Net architecture, our model achieves an excellent performance on simulated trajectories for both tasks without any prior knowledge of anomalous diffusion. The validation results demonstrate a mean absolute error (MAE) of the order of 0.01 for the prediction of dif-

* huangzih@hnu.edu.cn

fusion exponents, and an mDice coefficient approaching 1 for the segmentation of different dynamics models, outperforming alternative approaches such as recurrent neural networks (RNNs) [46, 47] and Transformers (TFMs) [48]. Moreover, the generalization ability of U-AnDi for real-world data is evaluated through experimental observations of the diffusion of transmembrane proteins on cell membrane surfaces [49]. The segmentation results exhibit a high degree of consistency with experimental observations, highlighting the applicability of our approach to characterizing anomalous diffusion in real complex systems.

This paper is organized as follows. Sec. II summarizes the details of two subtasks regarding the semantic segmentation of anomalous diffusion, and provides the methods for generating simulated trajectories. The architecture of U-AnDi model and its corresponding training scheme are described in Sec. III. The performance of U-AnDi on two subtasks is presented in Sec. IV. In Sec. V, we showcase the implementation of our method on experimental trajectories of transmembrane protein on membrane surfaces. Finally, we engage in a discussion and draw our conclusions in Sec. VI.

II. TASKS AND DATASETS

In this section, we present the details of two subtasks for the semantic segmentation of anomalous diffusion and corresponding simulated datasets used for model training and evaluation. These tasks aim to effectively address the challenge of capturing the intermittent transitions among different diffusion states. Data generation for both tasks is facilitated by utilizing the open-source Python package, *andi-datasets*, which is specifically designed for generating, managing, and analyzing anomalous diffusion trajectories [25, 50]. In particular, we primarily focus on 2D trajectory data in this work, as most experimental observations of anomalous diffusion are performed in 2D or quasi-2D environments.

A. Subtask 1: Segmentation of trajectories with varying diffusion exponents

The first subtask focuses on the segmentation of trajectories in which the sub-trajectories exhibit varying diffusion exponents. Here, the diffusion exponent α quantifies the relation between mean squared displacement (MSD) and time interval τ , written as

$$\text{MSD} \sim (\tau)^\alpha. \quad (1)$$

This exponent equals 1 in the description of standard Brownian motion. In anomalous diffusion, it can be either less than or greater than 1, corresponding to sub-diffusion and super-diffusion, respectively. In real-world scenarios, the diffusion exponent may not remain constant due to inevitable changes of interactions between

the random walker and its surroundings [34]. However, traditional statistical methods, which are based on the calculation of MSD, require sufficiently long trajectories to accurately determine the diffusion exponent. As a result, for anomalous diffusion trajectories with limited length scales, these conventional approaches face substantial difficulties when attempting to distinguish segments with different diffusion exponents.

To address this challenge, subtask 1 is designed to empower our model with the capability to identify these segments and predict their corresponding diffusion exponents. In detail, simulated segments are generated by the *andi-datasets* package within the theoretical framework of Fractional Brownian motion (FBM) [51]. This diffusion model describes an ergodic diffusion process that is driven by a fractional Gaussian noise, where the diffusion exponent α satisfies $0.05 \leq \alpha < 2$. Diffusion coefficients of these segments are set as 1.0, while diffusion exponents α are uniformly sampled from interval $[0.05, 2)$. After that, segments with a count of M are combined to form a trajectory of length L . The minimum length of each segment is set as 10, and the count M is randomly selected from the values 2, 3, 4, and 5. Representative example of a single simulated trajectory with $L = 500$ and $M = 5$ is illustrated in Fig. 1(a), where different segments are marked in distinct colors. Time evolution of this trajectory is depicted in Fig. 1(b) for both the x and y dimensions, indicating that the trajectory data exhibits typical time-series characteristics. Consequently, we assign the diffusion exponents of segments to each point as point-wise labels, leading to a point-wise regression task for our model. As shown in Fig. 1(c), these labels enable the clear identification of transition times (change-points) among different diffusion states. The main evaluation metric for this point-wise regression task is the MAE:

$$\text{MAE} = \frac{1}{NL} \sum_{i=1}^N \sum_{t=1}^L |\alpha_{i,t}^{\text{Pred}} - \alpha_{i,t}^{\text{GT}}|. \quad (2)$$

Here, N is the number of trajectories to be evaluated. For the i th trajectory at time step t , $\alpha_{i,t}^{\text{Pred}}$ and $\alpha_{i,t}^{\text{GT}}$ denote the predicted and ground truth values of the diffusion exponent, respectively.

B. Subtask 2: Segmentation of trajectories with different dynamics models

The second subtask aims to segment trajectories composed of segments, each with dynamics originating from a distinct diffusion model. It has been proven that the dynamics of anomalous diffusion is multifaceted and can be described by a variety of theoretical stochastic process models. Similar to the varying diffusion exponents in subtask 1, the anomalous diffusion dynamics observed in the real world often undergoes transitions due to changes or fluctuations in the surrounding media [33, 49]. For instance, the diffusion of transmembrane proteins on the

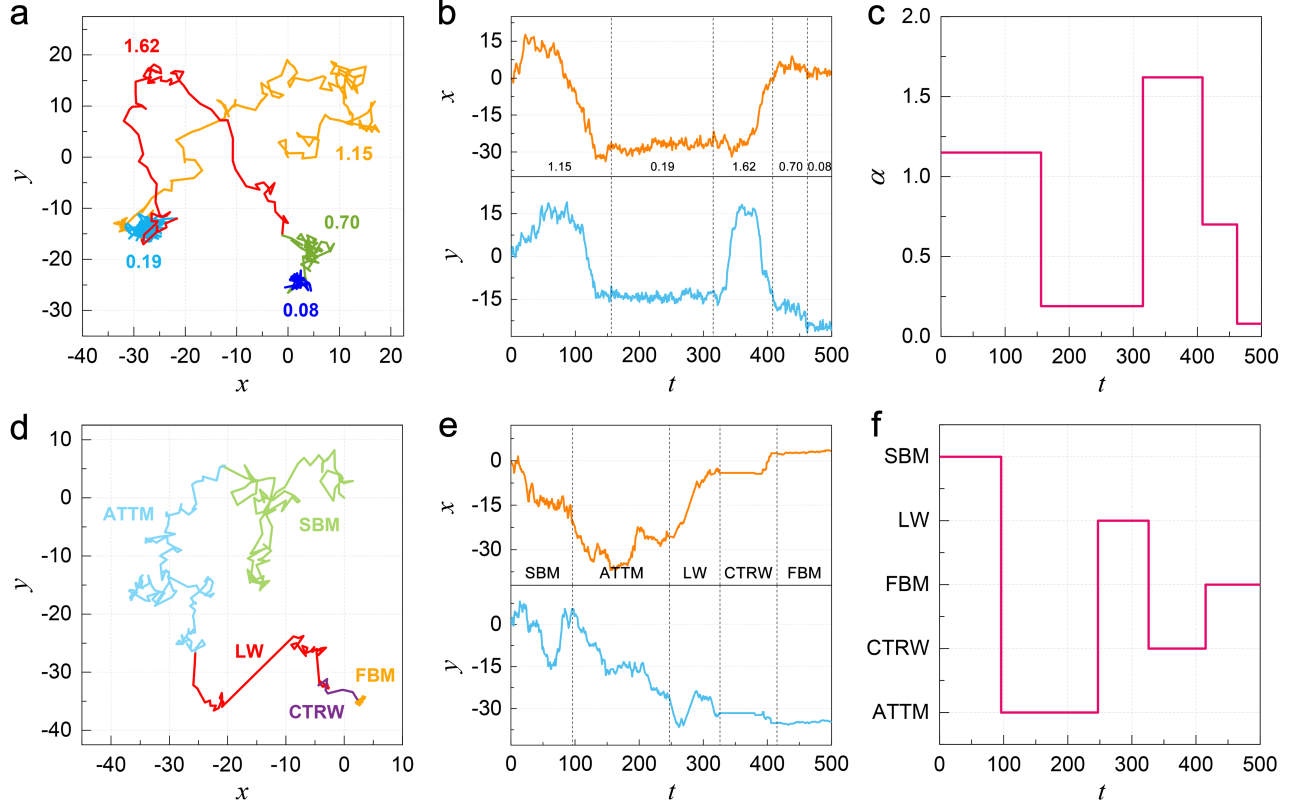


FIG. 1. [(a), (d)] Representative examples of trajectories with varying diffusion exponents (a) and different dynamics models (d). Different segments are marked in distinct colors. [(b), (e)] Time evolutions of trajectories in (a) and (d) for both x and y dimensions, respectively. Changepoints of diffusion states are indicated by dashed lines. [(c), (f)] Point-wise labels of trajectories in (a) and (d), respectively.

cell membrane surface [49, 52] exhibits a duality of dynamics, encompassing both FBM and continuous-time random walk (CTRW) [53]. However, traditional statistical methods are not particularly adept at identifying the dynamics model from raw trajectory data, and the detection of transitions among these dynamics proves even more challenging. Therefore, developing effective methods to address this issue bears considerable significance for the analysis of anomalous diffusion behaviors and the elucidation of underlying physical mechanisms.

For that purpose, we design the subtask 2 with the goal of enabling our model to detect state changepoints in the diffusion process and accurately identify the dynamics models of segments. Five theoretical diffusion models are considered:

- Annealed transient time motion (ATTM) [54]: Brownian motion with a diffusion coefficient that varies randomly in either time or space ($0.05 \leq \alpha \leq 1$).
- Continuous-time random walk (CTRW) [53]: The waiting time between two consecutive steps is irregular and randomly chosen ($0.05 \leq \alpha \leq 1$).
- Fractional Brownian motion (FBM) [51]: Diffusion

process driven by a power-law correlated fractional Gaussian noise ($0.05 \leq \alpha < 2$).

- Lévy walk (LW) [55]: The waiting time between subsequent steps is irregular, while the step length is not Gaussian distributed ($1 \leq \alpha \leq 2$).
- Scaled Brownian motion (SBM) [56]: Brownian motion with a deterministically time-dependent diffusion coefficient ($0.05 \leq \alpha \leq 2$).

Under the guidance of these 5 models, segments are generated using the *andi-datasets* package. The procedure for forming a trajectory in this subtask is the same as in subtask 1, with parameters including a trajectory length L and a count of segments M ranging from 2 to 5. As an illustrative example, we present a typical sample of a trajectory with $L = 500$ and $M = 5$ in Fig. 1(d) and its corresponding time evolution for both x and y dimensions in Fig. 1(e). This trajectory with different dynamics models is also labeled in a point-wise manner, as depicted in Fig. 1(f). Such a label results in a point-wise classification task, where the main evaluation metric we select is the mean Dice coefficient (mDice). The Dice coefficient, also known as the Sørensen-Dice coefficient, can measure the similarity of two samples and is com-

monly utilized in segmentation tasks [57]. This metric can be calculated in subtask 2 as:

$$\text{mDice} = \frac{1}{N} \sum_{i=1}^N \frac{2 \sum (\mathbf{X}_i^{\text{Pred}} \otimes \mathbf{X}_i^{\text{GT}})}{\sum \mathbf{X}_i^{\text{Pred}} + \sum \mathbf{X}_i^{\text{GT}}}. \quad (3)$$

Here, $\mathbf{X}_i^{\text{Pred}}$ is the predicted point-wise label and \mathbf{X}_i^{GT} refers to the ground truth of the i th trajectory. The symbol \otimes denotes the element-wise multiplication operator. Both $\mathbf{X}_i^{\text{Pred}}$ and \mathbf{X}_i^{GT} are one-hot encoded when performing the calculation of Dice coefficient. The value of the mean Dice coefficient ranges from 0 to 1, with a higher value indicating a better segmentation performance.

III. MODEL

A. Architecture of U-AnDi model

The U-AnDi model proposed in this work is constructed by integrating the WADNet encoder [45] into the U-Net architecture. Hence, we first introduce the encoder part of our segmentation model, which is designed based on the dilated causal 1D convolution [58]. In contrast to standard 1D convolution, causal convolution preserves the temporal causality when processing time-series data. In more detail, when applying the causal convolution to calculate the output at time step t , only the data from the preceding t steps in the previous layer will be used. This is achieved by applying padding on both sides of the sequence. However, the receptive field of a standard causal convolution is relatively small. To obtain a larger receptive field within a limited number of convolutional layers, dilated convolution should be performed simultaneously. A schematic representation of a dilated causal 1D convolution is given in Fig. 2(a), where the kernel size is set as 3. By doubling the dilation factor layer by layer, after applying convolutions for d (dilation depth) times, a single node can cover the information of $2^{d+1} - 1$ nodes in the input layer. This receptive field is significantly larger than that of a normal causal convolution ($2d + 1$), indicating a better capability to capture long-range dependencies in time-series data and reduce information loss during the down-sampling process.

The detailed structure of the network encoder is depicted in Fig. 2(b). The dilation depth d within the encoder is 5, and the filter number f for all convolutional layers in a single encoder are set to be the same. The input tensor \mathbf{x} initially passes through a standard causal convolution with a kernel size (ks) of 3. After that, the output \mathbf{x}_1 is processed by the subsequent layers, which consist of the gated activation unit and 1D convolutional layer with $ks = 1$, as highlighted by the rectangular dashed box in Fig. 2(b). Let \mathbf{x}_k represent the input of the k th layer where k ranges from 1 to d . The output of the k th layer \mathbf{h}_k can be written as:

$$\mathbf{h}_k = W^1 * [\tanh(W_{f,k} * \mathbf{x}_k) \otimes \sigma(W_{g,k} * \mathbf{x}_k)]. \quad (4)$$

Here, $*$ denotes the convolution operation, $\tanh(\cdot)$ and $\sigma(\cdot)$ refer to the hyperbolic tangent function and sigmoid function, respectively. W^1 represents the 1D convolution with $ks = 1$. $W_{f,k}$ and $W_{g,k}$ are independent dilated causal 1D convolutions with $ks = 3$ and dilation $= 2^{k-1}$. \mathbf{h}_k is directly used as the input of next $(k + 1)$ th layer, meaning $\mathbf{x}_{k+1} = \mathbf{h}_k$. The output \mathbf{z} of an encoder can be finally obtained by $\mathbf{z} = \mathbf{x}_1 + \sum_{k=1}^d \mathbf{h}_k$. For convenience, we denote the operation of WADNet encoder as $\mathcal{W}(\cdot)$, i.e., $\mathbf{z} = \mathcal{W}(\mathbf{x})$, in the following discussion.

By incorporating this encoder into the U-Net structure, we construct the U-AnDi model, with its architecture displayed in Fig. 2(c). The down-sampling block consists of a WADNet encoder, a batch normalization layer, and a max-pooling layer. We employ four consecutive down-sampling blocks to perform feature extraction on the input tensor. In the m th block, the input \mathbf{v}_m is processed as governed by:

$$\mathbf{u}_m = \text{BN}[\mathcal{W}_m(\mathbf{v}_m)], \quad (5)$$

$$\mathbf{v}_{m+1} = \text{MaxPool}(\mathbf{u}_m), \quad (6)$$

where $m = 1, 2, 3, 4$. BN and MaxPool represent the batch normalization [59] and max-pooling operators, respectively. The filter number f_m in encoder \mathcal{W}_m is $64 \times 2^{m-1}$ for subtask 1 and $128 \times 2^{m-1}$ for subtask 2. The pooling size of max-pooling layer is set as 2.

Next, the output from the 4th down-sampling block, \mathbf{v}_5 , is processed through five consecutive up-sampling blocks to generate full-resolution feature maps, which are then used for point-wise predictions. The up-sampling block is comprised of a WADNet encoder, a batch normalization layer, an up-sampling layer using the nearest neighbor algorithm, and a 1D convolutional layer with $ks = 1$. In particular, skip connections are applied to get the input \mathbf{p}_n of the n th up-sampling block when $n \geq 2$, as displayed by the dashed lines in Fig. 2(c). These connections serve to reduce the loss of fine-grained details during the up-sampling process and can be mathemati-

TABLE I. The shapes of intermediate tensors for subtask 2 when length of input trajectory is 500.

Tensor	Shape	Tensor	Shape
\mathbf{v}_1	[500, 2]	$\tilde{\mathbf{p}}_2$	[62, 1024]
\mathbf{v}_2	[250, 128]	\mathbf{p}_2	[62, 2048]
\mathbf{v}_3	[125, 256]	$\tilde{\mathbf{p}}_3$	[124, 512]
\mathbf{v}_4	[62, 512]	\mathbf{p}_3	[125, 1024]
$\mathbf{v}_5(\mathbf{p}_1)$	[31, 1024]	$\tilde{\mathbf{p}}_4$	[250, 256]
\mathbf{u}_1	[500, 128]	\mathbf{p}_4	[250, 512]
\mathbf{u}_2	[250, 256]	$\tilde{\mathbf{p}}_5$	[500, 128]
\mathbf{u}_3	[125, 512]	\mathbf{p}_5	[500, 256]
\mathbf{u}_4	[62, 1024]	\mathbf{p}_f	[500, 5]

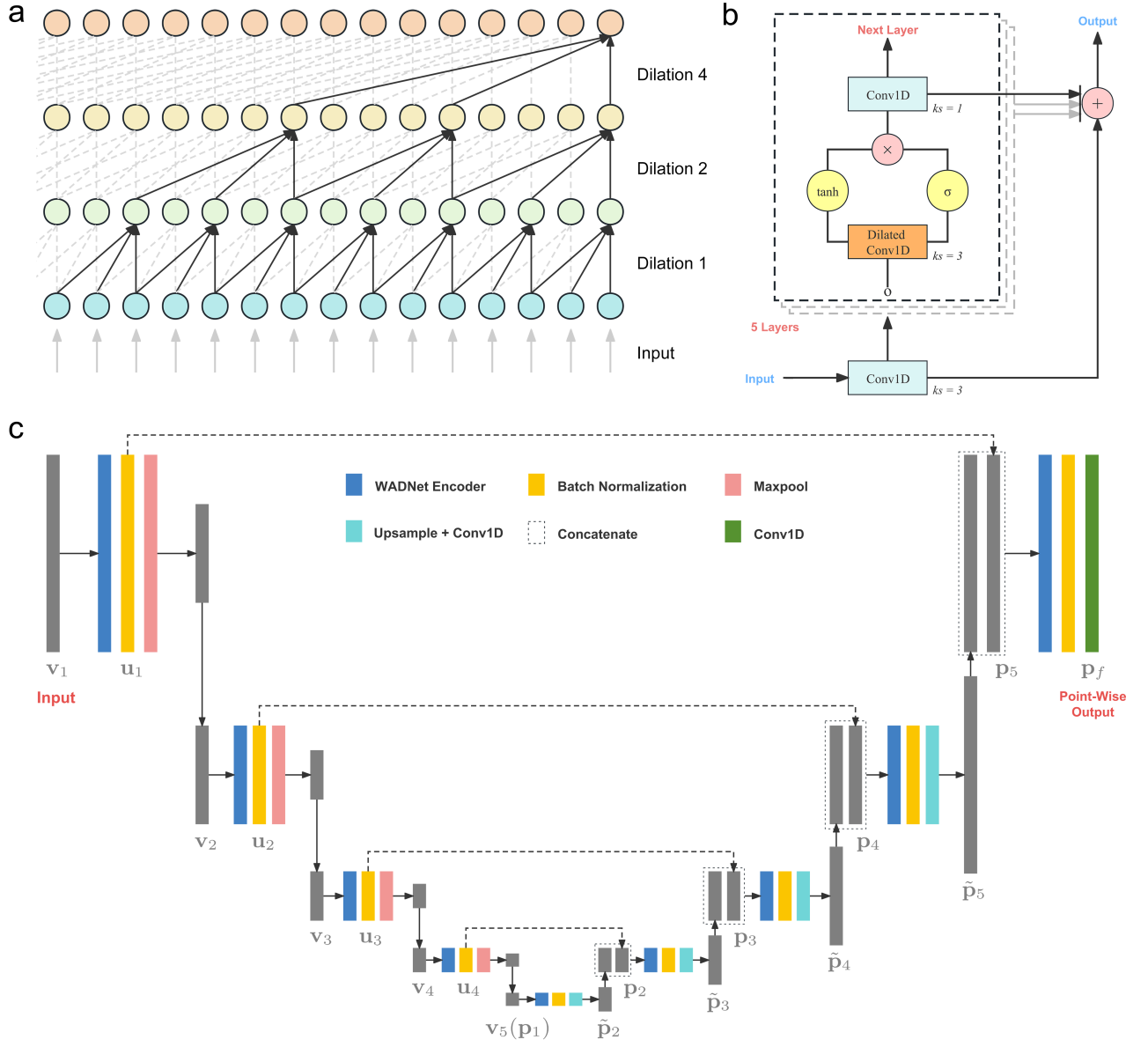


FIG. 2. (a) Schematic diagram of the dilated causal 1D convolution with a kernel size of 3. The dilation factor of convolution is doubled layer by layer. (b) Detailed structure of the WADNet encoder. (c) The architecture of our U-AnDi model. Skip connections are highlighted by the dashed lines.

cally described as:

$$\tilde{\mathbf{p}}_n = W_{n-1}^1 * \text{UP} \{ \text{BN} [\mathcal{W}_{n-1} (\mathbf{p}_{n-1})] \}, \quad (7)$$

$$\mathbf{p}_n = \text{Concat} (\tilde{\mathbf{p}}_n, \mathbf{u}_{6-n}), \quad (8)$$

where $n = 2, 3, 4, 5$ and $\mathbf{p}_1 = \mathbf{v}_5$. UP denotes the up-sampling operator, with a scale factor set as 2. Concat is the concatenation operator. The filter number f_n in encoder \mathcal{W}_n is $64 \times 2^{5-n}$ for subtask 1 and $128 \times 2^{5-n}$ for subtask 2. The filter number of the 1D convolutional layer W_n^1 is the half of that in encoder \mathcal{W}_n . Note that when performing the skip connection in Eq. (8), the shapes of $\tilde{\mathbf{p}}_n$ and \mathbf{u}_{6-n} may not necessarily match. In such cases, we apply padding to $\tilde{\mathbf{p}}_n$ to make it compati-

ble for concatenation with \mathbf{u}_{6-n} . In the last up-sampling block, the up-sampling layer is removed, and the filter number of the convolutional layer is adjusted (1 for subtask 1 and 5 for subtask 2). This yields a final output \mathbf{p}_f of the U-AnDi model, written as:

$$\mathbf{p}_f = W_5^1 * \text{BN} [\mathcal{W}_5 (\mathbf{p}_5)]. \quad (9)$$

To illustrate the details of the U-AnDi architecture more clearly, we take a trajectory with $L = 500$ as the input and present the shapes of intermediate tensors for subtask 2 in Table I. The shape follows the format: [length, channel]. For instance, the input tensor is obtained by concatenating the trajectory data from both x and y dimensions, leading to a shape of $[500, 2]$.

B. Training scheme and post-processing

To train our deep learning model, 1 000 000 trajectories are generated as the dataset for a fixed length parameter L . This dataset is randomly split into two parts: 80% for the training set and 20% for the validation set. The raw trajectory data is independently normalized along the x and y dimensions, achieving a mean of 0 and a standard deviation of 1 for each dimension. Then, the normalized data from both dimensions are concatenated and utilized as the input of the U-AnDi model. The selected loss functions are mean squared error (MSE) for subtask 1 and cross entropy (CE) for subtask 2, respectively. The model is trained using the back-propagation algorithm with a batch size of 512 on a single NVIDIA A100 GPU. The learning rate is 0.0002, and the optimizer is Adam. In particular, an L2 penalty is applied for subtask 2 with a weight decay of 2×10^{-5} . The training process lasts 100 epochs for subtask 1 and 200 epochs for subtask 2. The model performance on the validation set is evaluated every 1000 steps.

We use the trajectory data with $L = 500$ as the example to illustrate the evolution of loss function during training, as shown in Fig. 3(a) for subtask 1 and Fig. 3(b) for subtask 2. A rapid convergence of the train loss can be observed for both tasks, with the valid loss exhibiting a similar trend. This indicates that our model is fully capable of accomplishing both tasks without encountering over-fitting issues. Furthermore, the optimal weight of the U-AnDi model is determined based on the best metric achieved on the validation set. The epoch dependences of valid metrics for subtask 1 and 2 are presented in Figs. 3(c) and 3(d), respectively. As indicated by the yellow dot, the selected weight corresponds to the step where the best metric is reached.

The post-processing techniques used to obtain the final predictions for both subtasks are summarized below. In subtask 1, which is a point-wise regression task, the output \mathbf{p}_f from a trained U-AnDi model serves as the predicted diffusion exponents. To ensure a reasonable prediction with exponents ranging from 0.05 to 2, values outside the interval are clipped to the interval edges in \mathbf{p}_f . On the other hand, \mathbf{p}_f is transformed using the following equations in subtask 2 to address this point-wise classification task:

$$\mathbf{X}_i^{\text{Prob}} = \text{Softmax}(\mathbf{p}_{f,i}), \quad (10)$$

$$\mathbf{X}_i^{\text{Pred}} = \arg \max(\mathbf{X}_i^{\text{Prob}}). \quad (11)$$

Here, i denotes the i th trajectory. Softmax represents the softmax activation function. $\mathbf{X}_i^{\text{Prob}}$ and $\mathbf{X}_i^{\text{Pred}}$ are the predicted probability and label, respectively.

IV. ANALYSIS OF MODEL PERFORMANCE ON SIMULATED TRAJECTORIES

In this section, without loss of generality, we mainly focus on trajectories with a length of 500 as the exam-

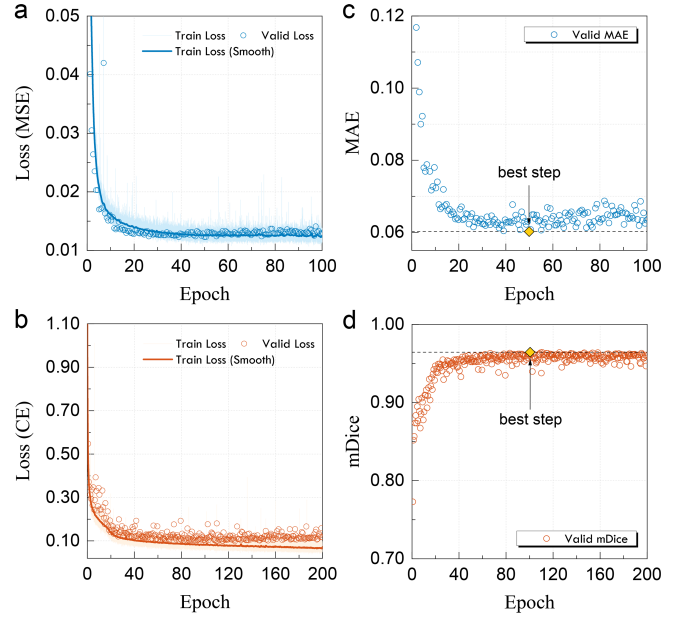


FIG. 3. (a)-(b) Evolution of the loss function during training for subtask 1 (a) and subtask 2 (b). The thick line represents a smoothed version of the original train loss to provide better visual guidance. (c)-(d) Epoch dependence of the valid metric for subtask 1 (c) and 2 (d). The dashed line denotes the value of the best metric, and the yellow dot highlights the location of the best step.

ple to demonstrate the performance of U-AnDi model on segmentation tasks of simulated trajectories. All results presented in this section are based on evaluations conducted on the validation sets for both subtasks, each containing 200 000 trajectories. In addition, for comparison purposes, we evaluate the performance of long short-term memory (LSTM) [46], gated recurrent unit (GRU) [47], and Transformer (TFM) [48] models on both subtasks. Each of these models is structured as a three-layered stack. The LSTM and GRU models both utilize a hidden state dimensionality of 64, while the TFM model employs an embedding space with a dimensionality of 128.

A. Performance of U-AnDi on subtask 1

To provide a more intuitive demonstration of U-AnDi's performance on subtask 1, we present four representative trajectories with segment counts $M = 2, 3, 4, 5$ in the left panel of Fig. 4, accompanied by comparisons of their predicted values and ground truth values in the right panel. It can be observed that the predicted diffusion exponents are quite close to the ground truth values, with only minor differences noticeable in a few short intervals. Quantitatively, as shown in Fig. 5(a), U-AnDi achieves an MAE of 0.06033 on the validation set, substantially outperforming the GRU (0.10967), LSTM (0.11433), and TFM (0.20080) models. On the other hand, the per-

formance of U-AnDi is also influenced by the trajectory length [Fig. 5(b)]. A longer trajectory leads to a smaller MAE, indicating a better model performance. This can be attributed to the longer average length of individual segments within the extended trajectories, which provides the model with more feature information.

For a fine-grained comparison between predictions and ground truths of diffusion exponents, we present the 2D

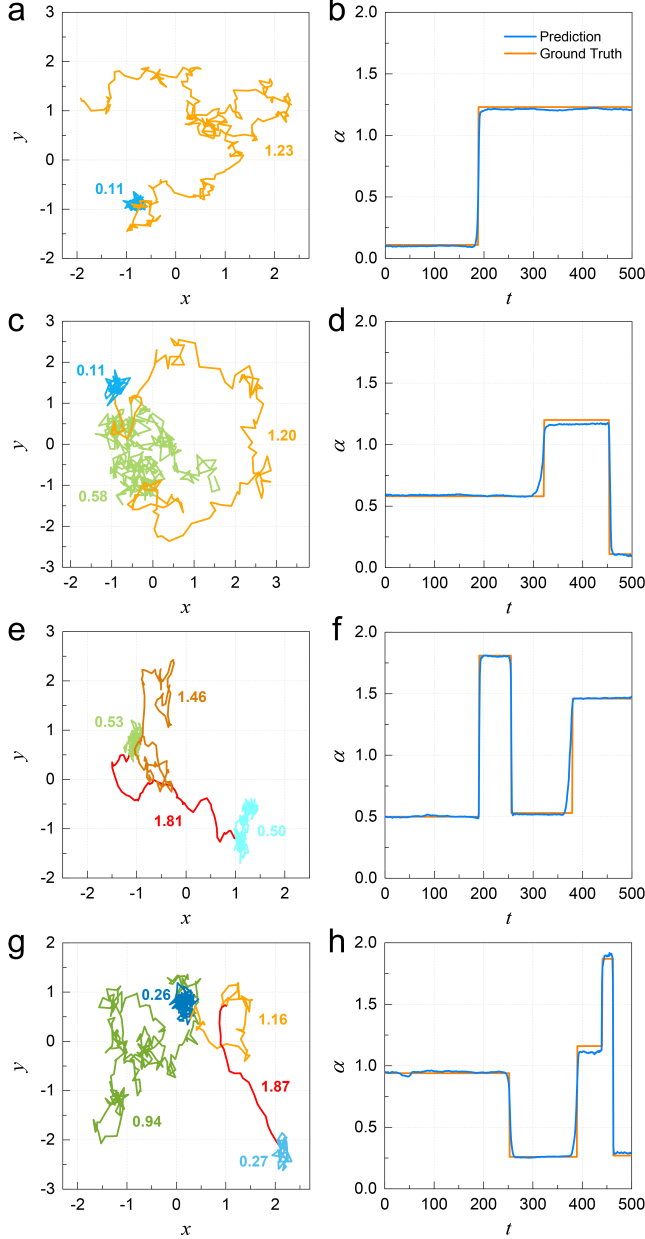


FIG. 4. Representative examples demonstrating U-AnDi's performance on subtask 1 for various segment counts M : (a)-(b) $M = 2$, (c)-(d) $M = 3$, (e)-(f) $M = 4$, (g)-(h) $M = 5$. Left panel: Trajectory visualizations, with segments of different diffusion exponents marked in distinct colors. Right panel: Comparisons between the predicted (blue) and ground truth (orange) diffusion exponents.

histogram of α^{Pred} versus α^{GT} in Fig. 5(c). As expected, the high-frequency pairs are predominantly located near the line $\alpha^{\text{Pred}} = \alpha^{\text{GT}}$, suggesting that the prediction errors of are small for all α^{GT} values ranging from 0.05 to 2. However, it should be noted that the prediction errors are not entirely uniform across different α^{GT} values. As displayed in Fig. 5(d), for α^{GT} values close to 0 or 2, the errors are relatively smaller, while for values around 1, the errors tend to be larger. In other words, for extreme subdiffusive or superdiffusive processes, their distinct motion characteristics allow for more accurate predictions of corresponding diffusion exponents. In contrast, for processes close to Fickian diffusion ($\alpha = 1$), with steps that are more likely to be completely random, the prediction accuracy of their diffusion exponents may be marginally reduced.

Besides the accuracy of predicting diffusion exponents, another crucial aspect is the identification of transition points (changepoints) among different diffusion states. As shown in the right panel of Fig. 4, the U-AnDi model, which generates continuous point-wise values as its output, enables an approximate visual determination of the changepoint ranges. However, its output cannot provide precise demarcations between successive distinct diffusion states, nor can it identify the associated diffusion exponents for individual segments. To address this challenge, we introduce a post-processing technique that converts the continuous point-wise predictions into discrete segmented predictions (See Appendix for details). An example of this process is illustrated in Fig. 5(e). After applying the post-processing, the predictions for all points within each segment become consistent, allowing for the identification of changepoints through the abrupt changes in diffusion exponents, as denoted by the dashed lines in Fig. 5(e). Based on this technique, we quantitatively investigate U-AnDi's performance on the detection of changepoints. We define δc as:

$$\delta c = c^{\text{Pred}} - c^{\text{GT}}, \quad (12)$$

where c^{Pred} and c^{GT} are the predicted and ground truth changepoints, respectively. Fig. 5(f) showcases the count distribution of δc for a range spanning from -9 to 9. It is evident that the majority of δc values are clustered around 0, signifying a relatively small error in the prediction of changepoints. Interestingly, the distribution demonstrates a mild leftward skew, which implies that the model has a slight inclination towards predicting changepoints earlier than their true positions. On the other hand, when performing the detection, the model may generate some non-existent changepoints (false positives, FPs), while potentially missing genuine changepoints (false negatives, FNs). Concerning the model-predicted changepoints, we classify those with $|\delta c| < 10$ as true positives (TPs) and those with $|\delta c| \geq 10$ as FPs. The counts of TPs, FPs, and FNs are shown in the inset of Fig. 5(f), where TPs constitute the vast majority of them. This result corresponds to a high F1-score [defined as $2\text{TP}/(2\text{TP} + \text{FP} + \text{FN})$] of 0.8750 with respect to the

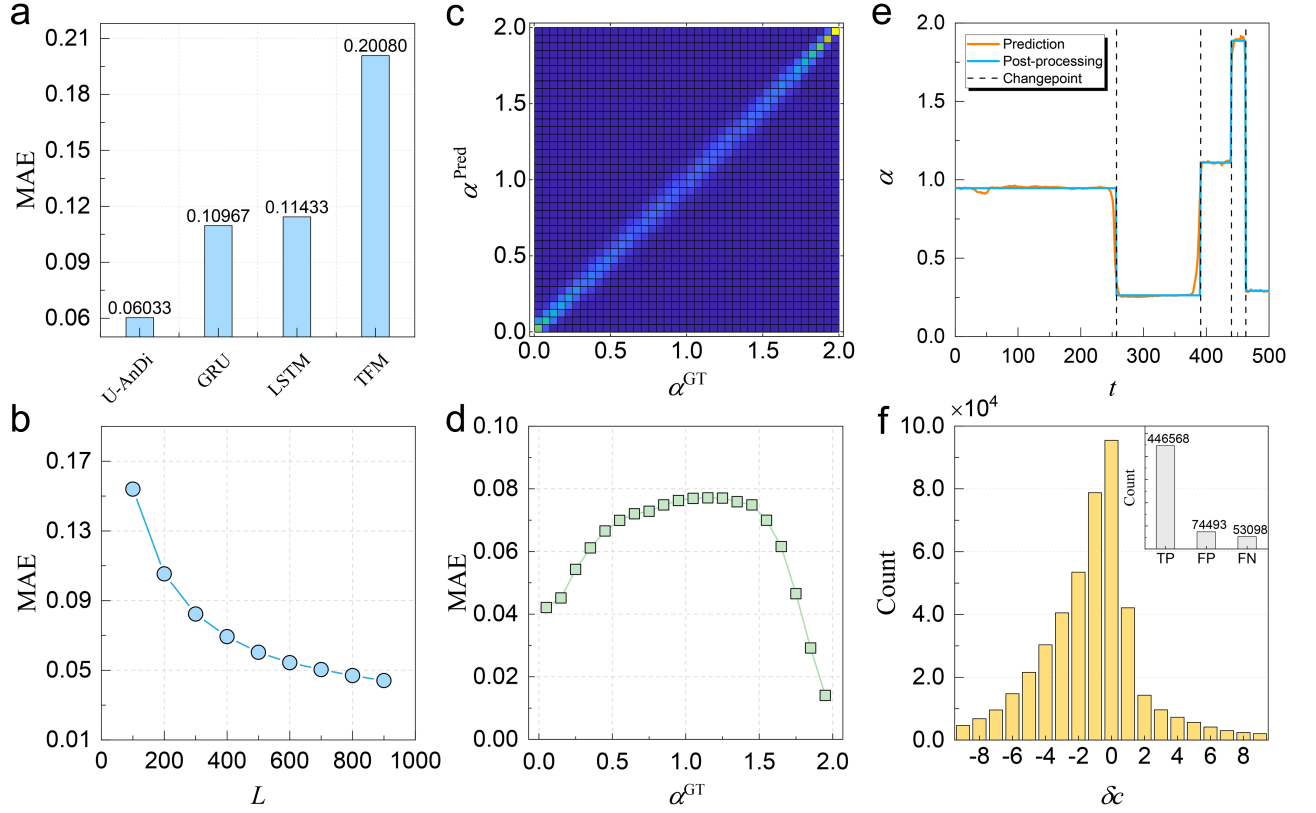


FIG. 5. (a) MAEs on the validation set for U-AnDi, GRU, LSTM, and TFM, with U-AnDi exhibiting the best performance. (b) U-AnDi’s performance on trajectories with different lengths. (c) 2D histogram of prediction α^{Pred} versus ground truth α^{GT} . (d) Distribution of MAE for α^{GT} values ranging from 0.05 to 2. (e) Representative example of the post-processing technique which converts the continuous point-wise predictions into discrete segmented predictions. The dashlines denote the predicted locations of changepoints. (f) The count distribution of δc for a range spanning from -9 to 9. Inset: Counts of TPs, FPs, and FNs for the detection of changepoints.

changepoint detection.

B. Performance of U-AnDi on subtask 2

In a manner consistent with subtask 1, we initially seek to visually demonstrate U-AnDi’s performance on the segmentation of trajectories with different dynamics models. For this purpose, the segmentation results of four representative trajectories with segment counts $M = 2, 3, 4, 5$ are summarized in Fig. 6. In more detail, Fig. 6 is organized into three rows for a coherent presentation. The first row [Figs. 6(a₁)-6(a₄)] presents the visualizations of these four trajectories, using unique colors to differentiate segments associated with distinct diffusion models. Subsequently, comparisons of predictions with ground truths for each of the four trajectories are displayed in the second row [Figs. 6(b₁)-6(b₄)]. It is evident that the lines depicting the predicted values (blue) closely align with those representing the ground truth values (orange). This highlights the robust performance of U-AnDi in dealing with the segmentation tasks with respect to different diffusion models. However, the

application of the argmax operator in Eq. (11) leads to a considerable loss of information in the predicted probability $\mathbf{X}_i^{\text{Prob}}$. In order to illustrate the information loss and provide a more comprehensive understanding of the model predictions, we show the heatmaps of point-wise probability distribution in the third row [Figs. 6(c₁)-6(c₄)], with darker colors representing values closer to 1. In the majority of instances, the model is capable of predicting the specific model at a given step with a high degree of confidence (probability). Nevertheless, there are occasional situations where competition among multiple models occurs. As demonstrated in Fig. 6(c₄), SBM and ATTM display comparable confidence values within the first segment.

For a more quantitative analysis, we calculate the mDice score of the U-AnDi model on the validation set. As presented in Fig. 7(a), our model achieves an mDice of 0.96450, greatly surpassing the performance of GRU (0.87780), LSTM (0.85253), and TFM (0.63052) models. Analogous to subtask 1, the performance of U-AnDi exhibits a positive correlation with the increasing trajectory length [Fig. 7(b)]. As can be observed, for trajectories with long lengths, the mDice value is in close proximity

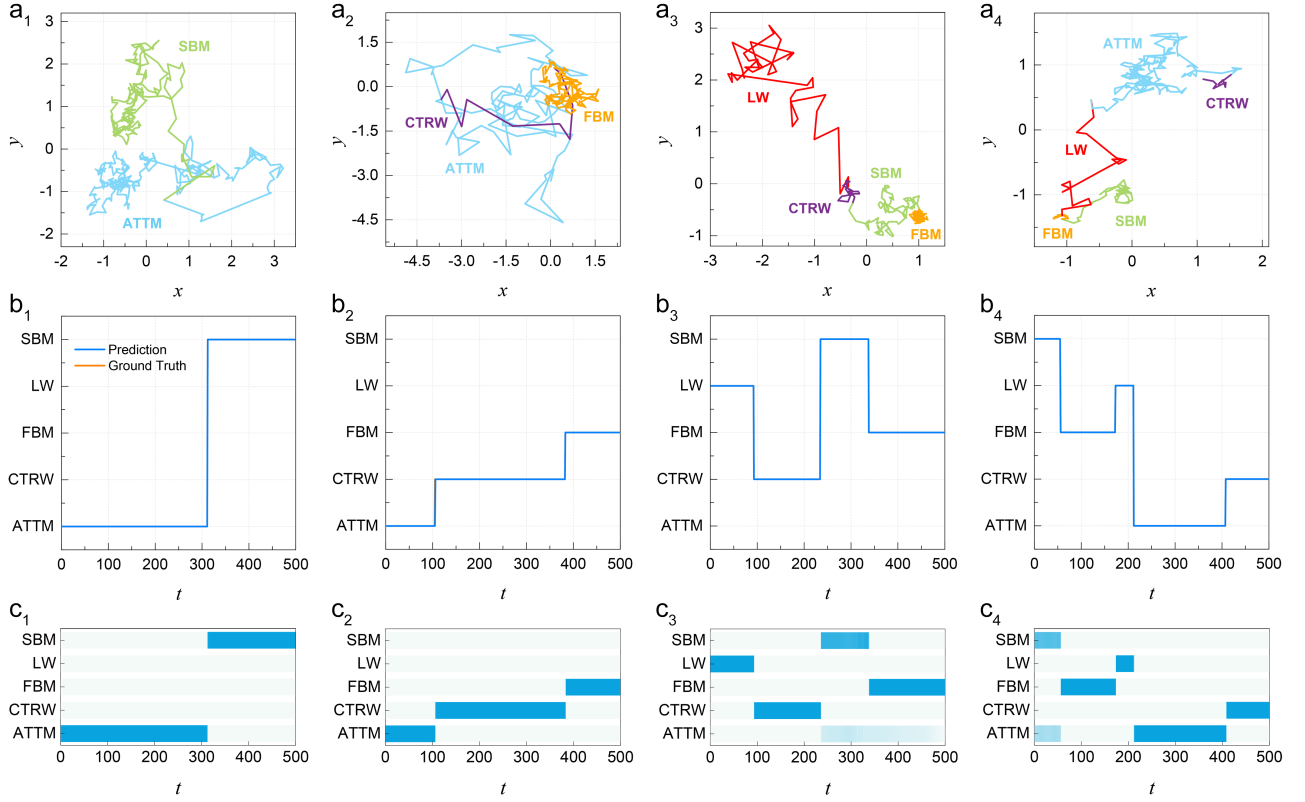


FIG. 6. Visualization of U-AnDi's performance on the segmentation task with different dynamics models. (a₁-a₄) Illustrations of four representative trajectories with varying segment counts ($M = 2, 3, 4, 5$), where different diffusion models are marked in distinct colors. (b₁-b₄) Comparisons of predictions (blue) and ground truths (orange) for each trajectory. The strong alignment between them leads to the near invisibility of lines representing ground truth values. (c₁-c₄) Heatmaps of point-wise probability distribution for each trajectory, with darker colors indicating higher probabilities.

to the full score 1. This indicates that our model exhibits exceptional capabilities in segmenting trajectories with different diffusion models. In addition, to gain a deep insight into the error origins regarding this point-wise classification task, the confusion matrix of classification results is displayed in Fig. 7(c). As revealed by the confusion matrix, in the case of the CTRW, FBM, LW, and SBM models, the classification accuracy surpasses 97%; however, the attained classification accuracy for the ATTM model is merely near 86%. This result is primarily due to the model's tendency to misclassify steps that ought to be ATTM, giving rise to erroneous predictions as CTRW (5.62%), FBM (3.68%), or SBM (4.55%). Consequently, the model demonstrates a diminished recall rate when addressing the segmentation of ATTM models.

On the other hand, detecting changepoints among multiple diffusion states holds significant importance in subtask 2 as well. In contrast to subtask 1, no additional post-processing techniques are required for the detection in this task. Instead, we can efficiently determine the positions of changepoints by examining abrupt changes in the predicted model labels. In line with our earlier approach, we utilize parameter δc to quantify the perfor-

mance of changepoint identifications. The count distribution of δc , with values ranging from -9 to 9, is depicted in Fig. 7(d). The finding reveals that in 91.1% of cases, the δc values are 0, signifying that a substantial portion of predicted changepoints are in perfect correspondence with ground truths. In particular, considering the highly imbalanced distribution of δc values, a logarithmic scale is applied to the counts in Fig. 7(d) to better visualize the distribution of δc . Simultaneously, the statistical results for TPs, FPs, and FNs, which share the same definitions as in subtask 1, are presented in the inset of Fig. 7(d). As expected, TPs constitute the majority, resulting in a high F1 score of 0.8957. This suggests that the U-AnDi model shows slightly improved capability in identifying changepoints in subtask 2 compared to subtask 1.

V. IMPLEMENTATION OF U-ANDI ON REAL-WORLD ANOMALOUS DIFFUSION DATA

In this section, we apply the U-AnDi model to real-world anomalous diffusion data and examine its performance on the semantic segmentation of experimental trajectories. The selected real-world system is the diffusion

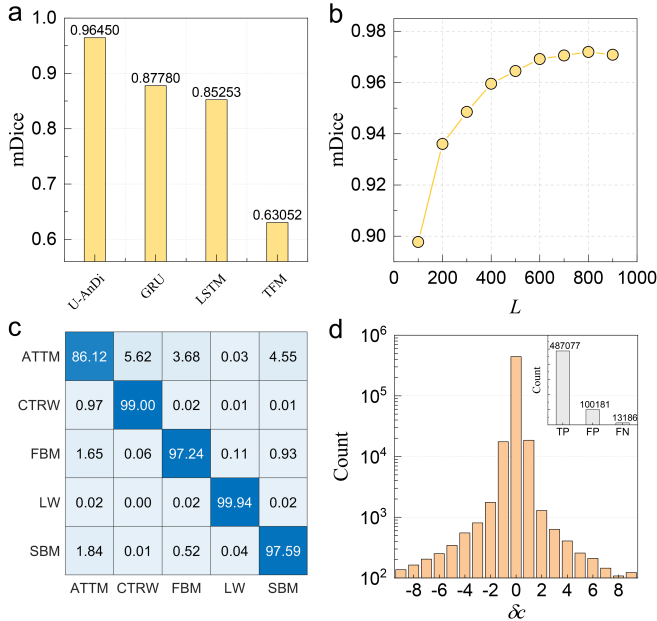


FIG. 7. (a) mDice scores on the validation set for U-AnDi, GRU, LSTM, and TFM, with U-AnDi outperforming the other three models. (b) mDice scores for different trajectory lengths. (c) Confusion matrix for the point-wise classification results, where horizontal and vertical coordinates denote predicted and ground truth labels, respectively. (d) Count distribution of δc ranging from -9 to 9, which is plotted on a logarithmic scale. Inset: Counts of TPs, FPs, and FNs for the detection of changepoints.

of transmembrane proteins on cell membrane surfaces, as illustrated by the schematic diagram in Fig. 8(a). The pertinent data are obtained through single-particle tracking techniques [60–64] from experimental observations, and are provided by N. Granik *et al.* in Ref. [49]. The content of this section is structured as follows. Sec. VA provides an overview of the raw experimental trajectory dataset, and describes the segmentation tasks along with the approach for preparing the validation set. The training strategy is outlined in Sec. VB. Finally, in Sec. VC, we demonstrate and discuss the performance of the U-AnDi model on interpreting the anomalous diffusion dynamics of transmembrane proteins.

A. Dataset description and segmentation tasks

The dataset with respect to the diffusion of transmembrane proteins on membrane surfaces comprises a total of 70221 2D trajectories, in which the x and y pixel locations are provided. The distribution of trajectory lengths is displayed in Fig. 8(b), with the counts plotted on a logarithmic scale to enhance clarity in visualization. An evident long tail distribution can be identified. In detail, trajectories of lengths no greater than 100 account for 98.6% (69259) of the entire dataset, while the maximum

length in this dataset reaches 1406. Diffusion models of these trajectories have been previously assessed by machine learning approaches in Ref. [49], with N. Granik *et al.* proposing that the predominant dynamics consist of both CTRW and FBM. Therefore, we utilize U-AnDi to process these experimental trajectories for the segmentation of different diffusion models.

Two specific segmentation tasks are addressed here: one involving labeled data and the other utilizing unlabeled data. In the task with labeled data, the validation set is prepared as below. Trajectories to be evaluated are generated by concatenating short trajectories with lengths not exceeding 100 from the experimental dataset. Diffusion-model labels of these short trajectories are assigned by WADNet, a deep learning model capable of providing the probability of the diffusion model to which the input trajectory is most likely to belong. Further details regarding WADNet can be found in our previous work [45]. Leveraging the model probabilities provided by WADNet for these short trajectories, we carefully select CTRW and FBM instances that exhibit high confidence levels (with probabilities of CTRW or FBM exceeding 0.9) to generate extended trajectories for further evaluation. Representative samples of these selected short trajectories with different lengths are illustrated in the inset of Fig. 8(b). The quantities of short CTRW and FBM trajectories spanning various lengths from 10 to 100 are presented in Fig. 8(c). By setting the overall trajectory length L and the number of concatenated segments M , we can utilize these short trajectories to create the validation set, thereby facilitating a comprehensive evaluation of U-AnDi’s performance. In particular, we establish a rule specifying that the average length of segments (L/M) should not exceed 50. This constraint ensures the prevention of trajectory generation errors or the dominance of overly long segments.

On the other hand, in the task concerning unlabeled data, we employ the U-AnDi model to segment those long trajectories with lengths exceeding 100. To examine the performance of our model, the segments distinguished by U-AnDi are classified by WADNet to identify their corresponding dynamics models. Due to the absence of ground truth labels, we cannot use a conventional evaluation metric like the mDice score to assess the segmentation results. Instead, we rely on the confidence levels (probabilities) provided by WADNet to evaluate the effectiveness of our model.

B. Training scheme

The architecture of the U-AnDi model and training methods in this section remains almost identical to those in subtask 2. One deviation is a reduction in the filter number of the last 1D convolutional layer from 5 to 2. This modification is due to the task at hand, which requires semantic segmentations of just two diffusion models, CTRW and FBM. Another update is the initializa-

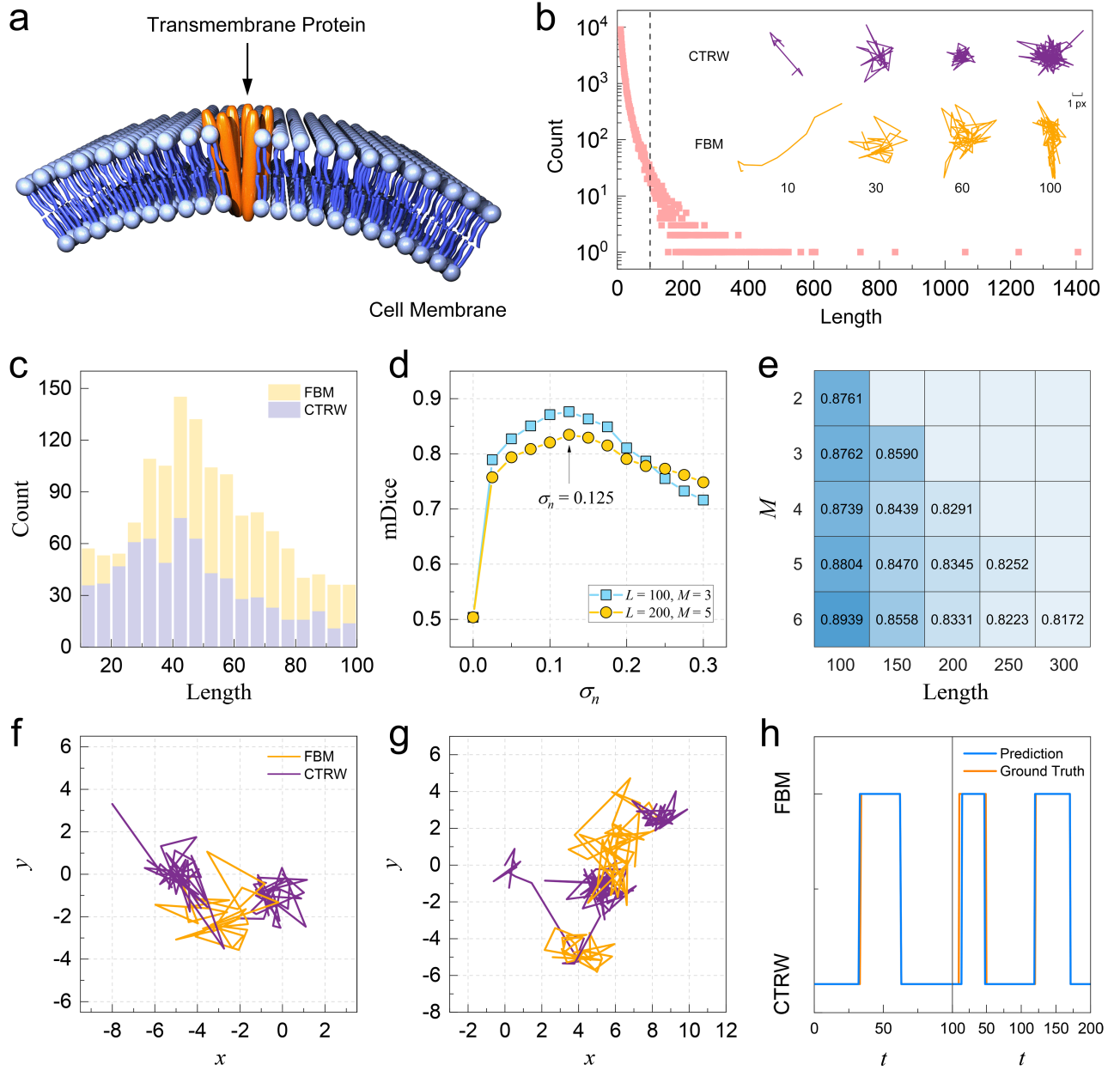


FIG. 8. (a) Schematic diagram of the selected real-world anomalous diffusion system: Diffusion of transmembrane proteins on cell membrane surfaces. (b) Logarithmically plotted distribution of trajectory lengths in the experimental dataset, with the dashed line denoting the length at 100. Inset: Representative instances of selected short trajectories of CTRW and FBM with different lengths, with labels assigned by WADNet. (c) The quantity distribution of short CTRW and FBM trajectories spanning various lengths from 10 to 100. (d) Segmentation performance of U-AnDi at different noise standard deviations σ_n . (e) mDice scores of U-AnDi on validation sets under diverse L and M parameters. (f)-(g) Trajectories from the validation sets with parameters $L = 100, M = 3$ in (f) and $L = 200, M = 5$ in (g). (h) Comparisons between the predictions (blue) and ground truths (orange) for the trajectory in (f) (left) and the trajectory in (g) (right), underscoring a high-level consistency.

tion of model weights. To accelerate the training process, we adopt a transfer learning strategy where the optimal model weights from subtask 2 are employed to initialize the model. This strategy allows the model to reach optimal performance within approximately 10 epochs, significantly reducing the training time.

In addition, taking the inevitable errors and noise

during experimental observations into account, Gaussian white noise with a zero mean and a standard deviation of σ_n is added when generating simulated trajectories for training. In order to pinpoint the optimal σ_n and better mimic the circumstances of real experimental data, we select two validation sets comprising of experimental trajectories to evaluate the performance of U-AnDi

at different σ_n . The parameters for these two validation sets are $L = 100, M = 3$ and $L = 200, M = 5$, respectively, with each set consisting of 1000 trajectories. As demonstrated in Fig. 8(d), for both validation sets, U-AnDi achieves the best performance (the highest mDice score) when $\sigma_n = 0.125$. Consequently, simulated trajectories with the standard deviation of noise $\sigma_n = 0.125$ are chosen to train the U-AnDi model in this section.

C. Performance of U-AnDi on two tasks regarding experimental trajectories

For the task involving labeled data, we investigate the performance of U-AnDi on validation sets with different parameters, as quantified by the mDice scores. The results are summarized in Fig. 8(e), where each validation set contains 1000 trajectories. It is observed that all mDice scores are above 0.8 for trajectory lengths ranging from 100 to 300, indicating an exceptional capability of U-AnDi in segmenting experimental trajectories. We also observe that segmentation performance improves as trajectory length decreases. Considering that trajectories with larger L are produced by concatenating longer segments, this finding might suggest that our model is more proficient at capturing shorter segments in real anomalous diffusion data. Moreover, to illustrate the segmentation results intuitively, we present two representative samples from the validation sets, along with their corresponding predicted labels, in Figs. 8(f) and 8(g). Comparisons between the predictions and ground truths of these two samples are presented in the left and right panels of Fig. 8(h), respectively, with a high degree of consistency being observed as expected.

Next, in the task with unlabeled data, we utilize the trained U-AnDi model to segment natural trajectories in the experimental dataset with lengths exceeding 100. In the absence of ground truth labels, we leverage WADNet to obtain probabilities of diffusion models for the segments identified by U-AnDi. To provide a concrete illustration of the model's effectiveness, three representative trajectories and their corresponding results are displayed in Fig. 9. As distinguished by the distinct colors, trajectories in Figs. 9(a)-9(c) are segmented by U-AnDi into 2, 3, and 4 segments, respectively. The corresponding probabilities of diffusion models for these segments are presented in Figs. 9(d)-9(f). Observations suggest that, for the majority of segments, the diffusion models with the highest confidence levels (probabilities) remain CTRW and FBM. Nevertheless, for the second segment of the trajectory in Fig. 9(c), SBM is identified by WADNet as the most probable diffusion model. The result derived from our analysis on the task involving unlabeled data affirms the conclusion of N. Granik *et al.* that the diffusion of transmembrane proteins on cell membranes primarily exhibits CTRW and FBM characteristics [49]. However, it also hints that this conclusion may not be a comprehensive description of the entire diffusion process, which

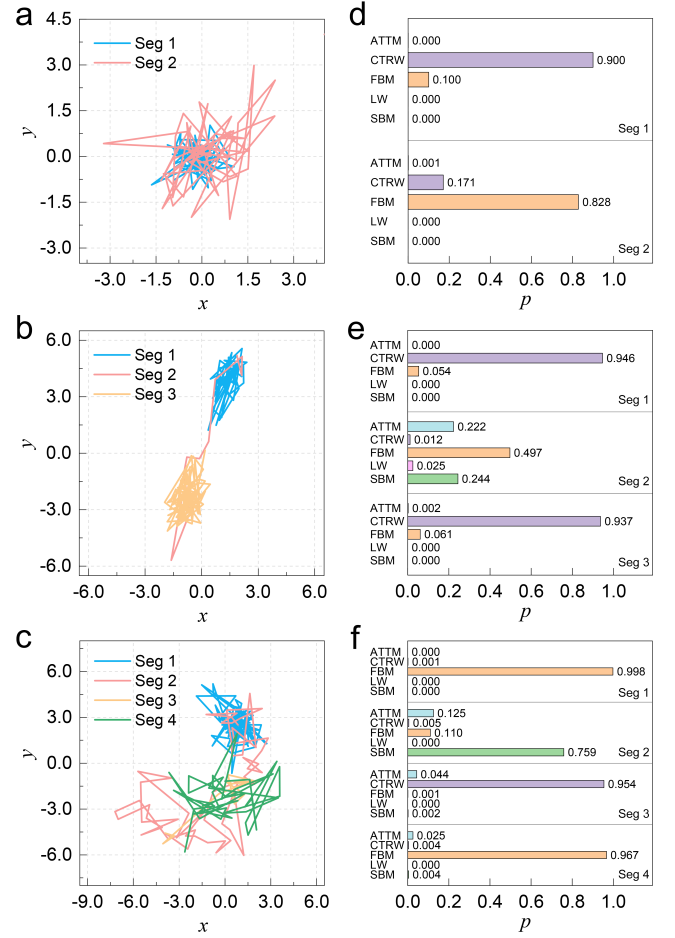


FIG. 9. (a)-(c) Representative natural trajectories from the experimental dataset with lengths surpassing 100. Segments identified by U-AnDi are distinguished by distinct colors. (d)-(f) Probabilities of diffusion models provided by WADNet for segments in (a)-(c), respectively.

could potentially entail a higher degree of complexity.

VI. CONCLUSION

By incorporating the WADNet encoder into the U-Net architecture, we develop a deep convolutional network, U-AnDi, to address the semantic segmentation of anomalous diffusion trajectories. Without requiring any prior knowledge of anomalous diffusion, our U-AnDi model demonstrates exceptional segmentation performance on simulated trajectories, whether they exhibit varying diffusion exponents or different dynamics models. The model achieves an MAE of the order of 0.01 in predicting diffusion exponents, and an mDice coefficient approaching 1 in segmenting diffusion models on the validation sets. This level of performance significantly surpasses that of both recurrent neural networks and Transformers. Further, U-AnDi also exhibits an excellent capability in dealing with the real-world anomalous diffusion

data, which is examined using the experimental dataset regarding the diffusion of transmembrane proteins on cell membrane surfaces. With the assistance of WADNet, the segmentation results show a high level of consistency with experimental observations, and potentially reveal a higher degree of complexity within the diffusion process. The supporting codes in this work are accessible at our GitHub repository [65].

Despite the promising performance of our model, there still exist opportunities for further refinements. The first is optimizing the detection of changepoints among different diffusion states. As displayed in the insets of Figs. 5(f) and 7(d), the current model could occasionally identify spurious transitions (FPs) and may also overlook genuine ones (FNs). Thus, reducing these inaccuracies is a critical task for future training and finetuning. Secondly, the implementation of U-AnDi is trained to recognize only five diffusion models in this study. Extending the model's ability to identify a larger variety of diffusion models would enhance the utility of U-AnDi in future research. Such an expansion would enable researchers to apply U-AnDi more effectively in the segmentation and property prediction of experimentally observed heterogeneous diffusion dynamics.

Additionally, it is important to note that the architecture of the U-AnDi model is not tied specifically to the framework of anomalous diffusion. It has the potential to be trained and perform segmentation tasks on other time-series datasets. In other words, our method not only provides a powerful and versatile tool for better understanding the dynamics of anomalous diffusion, but it also holds promise to be generalized as a universal scheme for the segmentation of time-series data.

ACKNOWLEDGMENTS

We thank Hui Zhao and Wentao Ju for helpful discussions. This work is supported by the National Natural Science Foundation of China (Grant No. 12104147) and the Fundamental Research Funds for the Central Univer-

sities.

Appendix: Post-processing technique in Subtask 1

Given a continuous point-wise prediction of diffusion exponents, denoted as:

$$\alpha_1, \alpha_2, \alpha_3, \dots, \alpha_L, \quad (\text{A.1})$$

for a trajectory of length L , we first calculate the differences between adjacent elements and get the sequence:

$$\beta_1, \beta_2, \beta_3, \dots, \beta_{L-1}, \quad (\text{A.2})$$

where $\beta_i = \alpha_{i+1} - \alpha_i$. Next, we set a threshold value ϵ ($\epsilon = 0.028$ in this work) and identify all indexes i satisfying $\beta_i > \epsilon$. These index form a new sequence:

$$i_1, i_2, i_3, \dots, i_k. \quad (\text{A.3})$$

If two consecutive indexes i_m and i_{m+1} in this sequence meet $i_{m+1} - i_m \geq 10$, we denote $i_m + 1$ as the starting point of the current segment, and i_{m+1} as the endpoint of this segment. Then, the changepoint between two successive predicted segments $[i_a + 1, i_{a+1}]$ and $[i_b + 1, i_{b+1}]$ can be identified in the interval $[i_{a+1} + 1, i_b]$. We select the point within this interval that exhibits the maximum absolute value of the derivative as the changepoint. Applying this rule, we can obtain the sequence of changepoints, given by:

$$c_1, c_2, c_3, \dots, c_n. \quad (\text{A.4})$$

Here, c_2, c_3, \dots, c_{n-1} are the predicted changepoints, and c_1 and c_n are set as 1 and L , respectively. Based on the detection result of changepoints, the predicted diffusion exponent $\tilde{\alpha}_i$ of the i th segment can be given as:

$$\tilde{\alpha}_i = \frac{1}{c_{i+1} - c_i} \sum_{j=c_i}^{c_{i+1}} \alpha_j, \quad (\text{A.5})$$

where $i = 1, 2, \dots, n - 1$.

-
- [1] R. Metzler, J.-H. Jeon, A. G. Cherstvy, and E. Barkai, Anomalous diffusion models and their properties: Non-stationarity, non-ergodicity, and ageing at the centenary of single particle tracking, *Phys. Chem. Chem. Phys.* **16**, 24128 (2014).
 - [2] J. Klafter and I. M. Sokolov, Anomalous diffusion spreads its wings, *Phys. World* **18**, 29 (2005).
 - [3] T. G. Mason and D. A. Weitz, Optical Measurements of Frequency-Dependent Linear Viscoelastic Moduli of Complex Fluids, *Phys. Rev. Lett.* **74**, 1250 (1995).
 - [4] F. D. A. A. Reis, Scaling relations in the diffusive infiltration in fractals, *Phys. Rev. E* **94**, 052124 (2016).
 - [5] G. Volpe and G. Volpe, The topography of the environment alters the optimal search strategy for active particles, *Proc. Natl. Acad. Sci. USA* **114**, 11350 (2017).
 - [6] Y. Sagi, M. Brook, I. Almog, and N. Davidson, Observation of Anomalous Diffusion and Fractional Self-Similarity in One Dimension, *Phys. Rev. Lett.* **108**, 093002 (2012).
 - [7] D. Hartich and A. Godec, Thermodynamic Uncertainty Relation Bounds the Extent of Anomalous Diffusion, *Phys. Rev. Lett.* **127**, 080601 (2021).
 - [8] E. Barkai, Y. Garini, and R. Metzler, Strange kinetics of single molecules in living cells, *Phys. Today* **65**, 29 (2012).
 - [9] Y. Ding, A. A. Hassanali, and M. Parrinello, Anomalous water diffusion in salt solutions, *Proc. Natl. Acad. Sci. USA* **111**, 3310 (2014).

- [10] J.-J. Song, R. Bhattacharya, H. Kim, J. Chang, T.-Y. Tang, H. Guo, S. K. Ghosh, Y. Yang, Z. Jiang, H. Kim, T. P. Russell, G. Arya, S. Narayanan, and S. K. Sinha, One-Dimensional Anomalous Diffusion of Gold Nanoparticles in a Polymer Melt, *Phys. Rev. Lett.* **122**, 107802 (2019).
- [11] Z. Xu, X. Dai, X. Bu, Y. Yang, X. Zhang, X. Man, X. Zhang, M. Doi, and L.-T. Yan, Enhanced heterogeneous diffusion of nanoparticles in semiflexible networks, *ACS Nano* **15**, 4608 (2021).
- [12] F. Höfling and T. Franosch, Anomalous transport in the crowded world of biological cells, *Rep. Prog. Phys.* **76**, 046602 (2013).
- [13] X.-L. Wu and A. Libchaber, Particle Diffusion in a Quasi-Two-Dimensional Bacterial Bath, *Phys. Rev. Lett.* **84**, 3017 (2000).
- [14] M. C. González, C. A. Hidalgo, and A.-L. Barabási, Understanding individual human mobility patterns, *Nature* **453**, 779 (2008).
- [15] B. Wang, J. Kuo, and S. Granick, Bursts of Active Transport in Living Cells, *Phys. Rev. Lett.* **111**, 208102 (2013).
- [16] P. Chen, Z. Huang, J. Liang, T. Cui, X. Zhang, B. Miao, and L.-T. Yan, Diffusion and directionality of charged nanoparticles on lipid bilayer membrane, *ACS Nano* **10**, 11541 (2016).
- [17] V. Plerou, P. Gopikrishnan, L. A. N. Amaral, X. Gabaix, and H. E. Stanley, Economic fluctuations and anomalous diffusion, *Phys. Rev. E* **62**, R3023 (2000).
- [18] J. Masoliver, M. Montero, and G. H. Weiss, Continuous-time random-walk model for financial distributions, *Phys. Rev. E* **67**, 021112 (2003).
- [19] Z.-Q. Jiang, W.-J. Xie, W.-X. Zhou, and D. Sornette, Multifractal analysis of financial markets: A review, *Rep. Prog. Phys.* **82**, 125901 (2019).
- [20] V. Sposini, D. Krapf, E. Marinari, R. Sunyer, F. Rittort, F. Taheri, C. Selhuber-Unkel, R. Benelli, M. Weiss, R. Metzler, *et al.*, Towards a robust criterion of anomalous diffusion, *Commun. Phys.* **5**, 305 (2022).
- [21] O. Vilk, E. Aghion, T. Avgar, C. Beta, O. Nagel, A. Sabri, R. Sarfati, D. K. Schwartz, M. Weiss, D. Krapf, R. Nathan, R. Metzler, and M. Assaf, Unravelling the origins of anomalous diffusion: From molecules to migrating storks, *Phys. Rev. Res.* **4**, 033055 (2022).
- [22] W. Wang, A. G. Cherstvy, R. Metzler, and I. M. Sokolov, Restoring ergodicity of stochastically reset anomalous-diffusion processes, *Phys. Rev. Res.* **4**, 013161 (2022).
- [23] H. Seckler and R. Metzler, Bayesian deep learning for error estimation in the analysis of anomalous diffusion, *Nat. Commun.* **13**, 6717 (2022).
- [24] B. Requena, S. Masó, J. Bertran, M. Lewenstein, C. Manzo, and G. Muñoz-Gil, Inferring pointwise diffusion properties of single trajectories with deep learning, *arXiv:2302.00410* (2023).
- [25] G. Muñoz-Gil, G. Volpe, M. A. Garcia-March, E. Aghion, A. Argun, C. B. Hong, T. Bland, S. Bo, J. A. Conejero, N. Firdas, *et al.*, Objective comparison of methods to decode anomalous diffusion, *Nat. Commun.* **12**, 6253 (2021).
- [26] C. Manzo, G. Muñoz-Gil, G. Volpe, M. A. Garcia-March, M. Lewenstein, and R. Metzler, Preface: Characterisation of physical processes from anomalous diffusion data, *J. Phys. A: Math. Theor.* **56**, 010401 (2023).
- [27] S. Bo, F. Schmidt, R. Eichhorn, and G. Volpe, Measurement of anomalous diffusion using recurrent neural networks, *Phys. Rev. E* **100**, 010102 (2019).
- [28] P. Kowalek, H. Loch-Olszewska, and J. Szwabiński, Classification of diffusion modes in single-particle tracking data: Feature-based versus deep-learning approach, *Phys. Rev. E* **100**, 032410 (2019).
- [29] N. Firdas, Óscar Garibó-i Orts, M. Ángel Garcia-March, and J. A. Conejero, Characterization of anomalous diffusion through convolutional transformers, *J. Phys. A: Math. Theor.* **56**, 014001 (2023).
- [30] G. Muñoz-Gil, G. G. i Corominas, and M. Lewenstein, Unsupervised learning of anomalous diffusion data: An anomaly detection approach, *J. Phys. A: Math. Theor.* **54**, 504001 (2021).
- [31] A. Gentili and G. Volpe, Characterization of anomalous diffusion classical statistics powered by deep learning (condor), *J. Phys. A: Math. Theor.* **54**, 314003 (2021).
- [32] A. Argun, G. Volpe, and S. Bo, Classification, inference and segmentation of anomalous diffusion with recurrent neural networks, *J. Phys. A: Math. Theor.* **54**, 294003 (2021).
- [33] K. Chen, B. Wang, and S. Granick, Memoryless self-reinforcing directionality in endosomal active transport within living cells, *Nat. Mater.* **14**, 589 (2015).
- [34] K. Chen, B. Wang, J. Guan, and S. Granick, Diagnosing heterogeneous dynamics in single-molecule/particle trajectories with multiscale wavelets, *ACS Nano* **7**, 8634 (2013).
- [35] F. Persson, M. Lindén, C. Unoson, and J. Elf, Extracting intracellular diffusive states and transition rates from single-molecule tracking data, *Nat. Methods* **10**, 265 (2013).
- [36] N. Monnier, Z. Barry, H. Y. Park, K.-C. Su, Z. Katz, B. P. English, A. Dey, K. Pan, I. M. Cheeseman, R. H. Singer, *et al.*, Inferring transient particle transport dynamics in live cells, *Nat. Methods* **12**, 838 (2015).
- [37] Y. Mo, Y. Wu, X. Yang, F. Liu, and Y. Liao, Review the state-of-the-art technologies of semantic segmentation based on deep learning, *Neurocomputing* **493**, 626 (2022).
- [38] K. He, G. Gkioxari, P. Dollor, and R. Girshick, Mask R-CNN, in *Proceedings of the IEEE International Conference on Computer Vision (ICCV)* (IEEE Computer Society, Venice, 2017) pp. 2961–2969.
- [39] T.-Y. Lin, P. Dollár, R. Girshick, K. He, B. Hariharan, and S. Belongie, Feature pyramid networks for object detection, in *Proceedings of the IEEE Conference on Computer Vision and Pattern Recognition (CVPR)* (IEEE Computer Society, Honolulu, Hawaii, 2017) pp. 2117–2125.
- [40] V. Badrinarayanan, A. Kendall, and R. Cipolla, SegNet: A deep convolutional encoder-decoder architecture for image segmentation, *IEEE Trans. Pattern Anal. Mach. Intell.* **39**, 2481 (2017).
- [41] L.-J. Li, R. Socher, and F.-F. Li, Towards total scene understanding: Classification, annotation and segmentation in an automatic framework, in *2009 IEEE Conference on Computer Vision and Pattern Recognition* (IEEE Computer Society, Miami, Florida, 2009) pp. 2036–2043.
- [42] O. Ronneberger, P. Fischer, and T. Brox, U-Net: Convolutional networks for biomedical image segmentation, in *Medical Image Computing and Computer-Assisted Intervention – MICCAI 2015* (Springer International Publishing, Cham, 2015) pp. 234–241.

- [43] M. Antonelli, A. Reinke, S. Bakas, K. Farahani, A. Kopp-Schneider, B. A. Landman, G. Litjens, B. Menze, O. Ronneberger, R. M. Summers, *et al.*, The medical segmentation decathlon, *Nat. Commun.* **13**, 4128 (2022).
- [44] G. Du, X. Cao, J. Liang, X. Chen, and Y. Zhan, Medical image segmentation based on U-Net: A review, *J. Imaging Sci. Technol.* **64**, 020508 (2020).
- [45] D. Li, Q. Yao, and Z. Huang, WaveNet-based deep neural networks for the characterization of anomalous diffusion (WADNet), *J. Phys. A: Math. Theor.* **54**, 404003 (2021).
- [46] S. Hochreiter and J. Schmidhuber, Long short-term memory, *Neural Comput.* **9**, 1735 (1997).
- [47] K. Cho, B. van Merriënboer, C. Gulcehre, D. Bahdanau, F. Bougares, H. Schwenk, and Y. Bengio, Learning phrase representations using RNN encoder–decoder for statistical machine translation, in *Proceedings of the 2014 Conference on Empirical Methods in Natural Language Processing (EMNLP)* (Association for Computational Linguistics, Doha, Qatar, 2014) pp. 1724–1734.
- [48] A. Vaswani, N. Shazeer, N. Parmar, J. Uszkoreit, L. Jones, A. N. Gomez, L. Kaiser, and I. Polosukhin, Attention is all you need, in *Proceedings of the 31st International Conference on Neural Information Processing Systems*, Vol. 30 (Curran Associates Inc., Red Hook, NY, 2017) p. 6000–6010.
- [49] N. Granik, L. E. Weiss, E. Nehme, M. Levin, M. Chein, E. Perlson, Y. Roichman, and Y. Shechtman, Single-particle diffusion characterization by deep learning, *Biophys. J.* **117**, 185 (2019).
- [50] G. Muñoz-Gil, B. Requena, G. Volpe, M. A. Garcia-March, and C. Manzo, Andichallenge/andi_datasets: Challenge 2020 release (v.1.0). zenodo. (2021).
- [51] B. B. Mandelbrot and J. W. V. Ness, Fractional Brownian motions, fractional noises and applications, *SIAM Rev.* **10**, 422 (1968).
- [52] M. Chein, E. Perlson, and Y. Roichman, Flow arrest in the plasma membrane, *Biophys. J.* **117**, 810 (2019).
- [53] H. Scher and E. W. Montroll, Anomalous transit-time dispersion in amorphous solids, *Phys. Rev. B* **12**, 2455 (1975).
- [54] P. Massignan, C. Manzo, J. A. Torreno-Pina, M. F. García-Parajo, M. Lewenstein, and G. J. Lapeyre, Nonergodic Subdiffusion from Brownian Motion in an Inhomogeneous Medium, *Phys. Rev. Lett.* **112**, 150603 (2014).
- [55] J. Klafter and G. Zumofen, Lévy statistics in a Hamiltonian system, *Phys. Rev. E* **49**, 4873 (1994).
- [56] S. C. Lim and S. V. Muniandy, Self-similar Gaussian processes for modeling anomalous diffusion, *Phys. Rev. E* **66**, 021114 (2002).
- [57] L. R. Dice, Measures of the amount of ecologic association between species, *Ecology* **26**, 297 (1945).
- [58] A. van den Oord, S. Dieleman, H. Zen, K. Simonyan, O. Vinyals, A. Graves, N. Kalchbrenner, A. Senior, and K. Kavukcuoglu, WaveNet: A generative model for raw audio, arXiv:1609.03499 (2016).
- [59] S. Ioffe and C. Szegedy, Batch normalization: Accelerating deep network training by reducing internal covariate shift, in *Proceedings of the 32nd International Conference on International Conference on Machine Learning - Volume 37* (JMLR.org, Lille, France, 2015) pp. 448–456.
- [60] C. Manzo and M. F. Garcia-Parajo, A review of progress in single particle tracking: From methods to biophysical insights, *Rep. Prog. Phys.* **78**, 124601 (2015).
- [61] H. Shen, L. J. Tauzin, R. Baiyasi, W. Wang, N. Moringo, B. Shuang, and C. F. Landes, Single particle tracking: From theory to biophysical applications, *Chem. Rev.* **117**, 7331 (2017).
- [62] H. Qian, M. Sheetz, and E. Elson, Single particle tracking. Analysis of diffusion and flow in two-dimensional systems, *Biophys. J.* **60**, 910 (1991).
- [63] M. J. Saxton, Single-particle tracking: Connecting the dots, *Nat. Methods* **5**, 671 (2008).
- [64] J. A. Torreno-Pina, C. Manzo, and M. F. Garcia-Parajo, Uncovering homo- and hetero-interactions on the cell membrane using single particle tracking approaches, *J. Phys. D: Appl. Phys.* **49**, 104002 (2016).
- [65] huangzih/U-AnDi, <https://github.com/huangzih/U-AnDi>.